Editors' Suggestion

Competing Magnetic Anisotropy and Domain-Wall Density for Optimizing Magnetization-Induced Water-Oxidation Enhancement

Anke Yu,[1,*] Durgesh Kumar,[2,*] Zizhao Gong,[3] Leonhard Tannesia,[1,4] Hasibur Rahaman,[2] Pengfei Song,[1] Tianze Wu,[1] Ramu Maddu,[2] Pinkesh Kumar Mishra,[2] Xiao Renshaw Wang,[2,5] S. N. Piramanayagam,[2,†] and Zhichuan J. Xu[1,6,‡]

[1]*School of Materials Science and Engineering, Nanyang Technological University, 50 Nanyang Avenue, Singapore 639798, Singapore*
[2]*School of Physical and Mathematical Sciences, Nanyang Technological University, 21 Nanyang Link, Singapore 637371, Singapore*
[3]*Beijing National Center for Condensed Matter Physics and Institute of Physics, Chinese Academy of Sciences, Beijing 100190, China*
[4]*Nanyang Environment and Water Research Institute (NEWRI), Interdisciplinary Graduate Programme, Nanyang Technological University, 1 Cleantech Loop, Singapore 637141, Singapore*
[5]*School of Electrical and Electronic Engineering, Nanyang Technological University, Singapore 637371, Singapore*
[6]*The Centre of Advanced Catalysis Science and Technology, Nanyang Technological University, Singapore 639798, Singapore*

(Received 22 May 2025; accepted 7 January 2026; published 11 March 2026)

The application of a magnetic field has emerged as an effective method for studying the spin-related effects in the oxygen evolution reaction (OER). However, the presence of spin-unrelated effects under a magnetic field also contributes to the observed OER increment, complicating the identification of spin-related enhancement. This is primarily associated with the intrinsic limitation of the conventional magnetic catalysts that require the continuous application of an external magnetic field to maintain the magnetization. Here, we have developed magnetron-sputtered Co/PtCo multilayer catalysts with perpendicular magnetic anisotropy, enabling a stable magnetization state without continuous magnetic fields. The magnetic anisotropy of the multilayers is controlled through the number of repetitions of Co/PtCo bilayers. As the bilayer number increases from 2 to 25, the domain size at the demagnetized state gradually reduces to the nanometer scale due to the enhanced magnetostatic energy. Upon premagnetization with out-of-plane magnetic fields, the pure spin-enhanced OER is numerically correlated to the change in domain wall ratios, where the global non-spin-related enhancement is effectively excluded. Such spin-enhanced OER is found to be favored by magnetic anisotropy due to the higher magnetic stability to maintain the magnetization state. This Letter provides a new strategy for achieving stable spin-related OER enhancement by magnetic anisotropy, advancing magnetic-field-free spin electrocatalysts to optimize OER performance.

DOI: 10.1103/bdr5-bg1j

Introduction—The oxygen evolution reaction (OER) is critical for the overall energy efficiency of water splitting. However, the reaction kinetics are intrinsically hindered by the thermodynamic limitation from the scaling relationship in the adsorption energy of intermediates [1,2]. Earlier theoretical works have found that manipulating the spin-related interactions in materials is a potential method to bypass the scaling relationship, which facilitates the spin-electron transfer to produce triplet-state oxygen [3,4]. Recent experimental studies demonstrated that the spin polarization induced by magnetic fields can enhance OER in ferromagnetic (FM) catalysts [5–8]. The enhancement effect has been correlated to the reformation of magnetic domains [9], on which the O−O coupling process is optimized by the FM exchange interaction [10,11]. However, the commonly used magnetic catalysts possess low magnetic hardness (or stability), indicating their magnetization state cannot be retained over time without external fields due to thermal fluctuations [12]. As a result, a continuous external magnetic field is required to sustain the OER enhancement, which hinders practical applications in real electrochemistry systems [13]. Besides, performing OER under an external magnetic field may induce multiple non-spin-related effects that could exaggerate the observed enhancement, which impedes accurate understanding of spin effects [14]. Therefore, it is significant to develop magnetic materials with intrinsically high magnetic stability, which can maintain their magnetization state for improving spin-related OER kinetics at magnetic-field-free conditions.

In a simplistic description, the magnetic hardness (or stability) of a magnetic material is usually proportional to

*These authors contributed equally to this work.
†Contact author: prem@ntu.edu.sg
‡Contact author: xuzc@ntu.edu.sg

Published by the American Physical Society under the terms of the Creative Commons Attribution 4.0 International license. Further distribution of this work must maintain attribution to the author(s) and the published article's title, journal citation, and DOI.

the anisotropy constant (K_u) [12,15]. Materials with low K_u, such as the typical FM OER catalysts, have in-plane magnetic anisotropy (IMA) and are magnetically soft [12], thus cannot retain magnetization after field removal. In contrast, materials with perpendicular magnetic anisotropy (PMA) normally have a higher anisotropy constant. Therefore, they are magnetically hard [12], making them promising for external field-free magnetic-enhanced OER. In the past decades, PMA films have received much interest in the spintronics community for their application in recording media and magnetic memory devices [12,15,16]. A well-established system to introduce PMA is the periodic stacking of FM (like Co) and nonmagnetic thin films (like Pt and Pd) [17], where PMA originates from the interface anisotropy by the abundance of interfaces [18]. In this system, the anisotropy and the domain structures could easily be tuned by the layer thickness and repetition.

Inspired by this, we developed the $(\mathrm{Co/PtCo})_{N-1}$ multilayer films with different numbers of bilayers (N) to produce distinctive magnetic anisotropy and remanent magnetization (M_r), which exhibits stable spin-related OER enhancement under pre-magnetization. The reported magnetic OER catalysts, such as magnetic nanoparticles ($CoFe_2O_4$ [6], $NiZnFeO_x$ [5], Fe_3O_4 [19], etc.) and in-plane anisotropic films (NiFe [9], $La_{0.67}Sr_{0.33}MnO_3$ [8], etc.), often lack strong magnetic anisotropy and retention at the remanence [6], hindering their potential in investigating spin-related OER mechanisms and developing magnetic field-free water splitting technologies. On the other hand, by performing pre-magnetization on the PMA films, the OER enhancement from the spin-related effect is distinguished from the non-spin-related effects, and spin-related enhancements are numerically linked to domain wall disappearance. To identify the spin-related contribution, we monitored the magnetization change in catalysts after removing the magnetic fields. The spin-related enhancement is found to be controlled by both the K_u and domain wall ratios, where moderate K_u with higher domain wall ratios favors the enhancement. Besides, the spin-related OER enhancement varied across different overpotentials, which we attribute to the different magnetic responses in distinct reaction pathways. Overall, this Letter provides a new strategy utilizing magnetic anisotropy in catalysts for achieving magnetic-field-free spin-enhanced OER, providing deeper insight into spin-related effects and the potential application in spintronic-driven energy conversion technologies.

Magnetization-caused OER increment—We employed a series of ultrathin Co/PtCo multilayers with carefully designed PMA, which has a lamination of $\mathrm{Ta(3)/Pt(5)/[Co(0.5)/PtCo(0.8)]_{N-1}Co(0.5)}$ (thicknesses in nm). The N is varied from 2 to 25 to control the strength of the PMA of the films, denoted as N2, N5, …N25 [20,21]. Appendix A elucidates the structure and chemical composition of the multilayers. In Appendix B, we show the decreased domain size and tunable PMA by increasing the N.

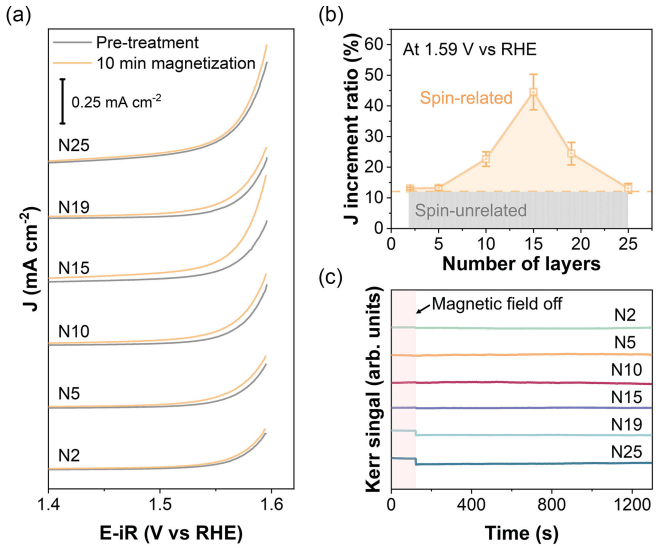


FIG. 1. (a) The OER CV for all multilayers before and after being magnetized to saturation for 10 min. (b) The OER current density increment ratio at 1.59 V vs RHE after the magnetization. The error bars represent the standard deviation from three independent tests. (c) Magnetization stability taken from MOKE for 20 min after turning off the magnetic field.

We then performed the OER by magnetization for the as-prepared films in 1 M KOH using a homemade cell with a three-electrode configuration (Supplemental Material Fig. 1 [22]). Previous studies commonly perform the OER directly under the magnetic field. However, the magnetic field can also affect the electrochemical performance by various effects [14], including bubble removal by magnetohydrodynamic (MHD) effect, magnetoresistance, magnetic heating, etc., which can interfere with the accuracy of the estimated magnetic field-enhanced OER. Therefore, in our practice, we avoid directly performing OER under an external magnetic field. Instead, we compare the change in OER activity before and after magnetizing the films. An electromagnet is adapted to produce a static magnetic field in a direction perpendicular to the film surface, sufficient to achieve saturation magnetization in all films. Cyclic voltammetry (CV) profiles were recorded for the stabilized $(\mathrm{Co/PtCo})_{N-1}$ multilayers before and after 10 min of magnetization (Supplemental Material [22]). After the magnetization, the OER current densities showed different improvements for multilayers with different N [Fig. 1(a)]. The magnetization-caused enhancement ratio is shown in Fig. 1(b), where the improvements for all films are below 50%, and the highest enhancement ratio is found in N15. The ratio enhances as N increases to 15 and then reduces for higher values of N. The change in charge transport from electrochemical impedance spectroscopy (EIS) measurement after magnetization also follows a similar trend (Supplemental Material Fig. 2 [22]), confirming the magnetic enhancement effect in OER. It is important to note that although the N2 showed a large domain structure, it also exhibits a small OER enhancement (~13%) by

magnetization, which is attributed to the non-spin-related effects. This non-spin-related enhancement is further elucidated by antiferromagnetic (AFM) CoOOH catalysts in Supplemental Material Figs. 3 and 4 [22].

Furthermore, the OER CV showed good stability for 5 cycles after magnetization (Supplemental Material Fig. 5 [22]), which correlates well with the good magnetization stabilities due to the high anisotropy of these samples [Fig. 1(c)]. All films retain their M_r for at least 20 min with 0 fields (Supplemental Material Fig. 6 [22]). It indicates that the improvement in OER activity is only triggered by the corresponding retentivity of films. Notably, the magnetizations of N19 and N25 drop to 26.6% and 14.2% with respect to their respective M_S after field removal, whereas all other films can retain at least $0.98M_S$. The relative M_r reflects the net magnetic moment of the film in the absence of magnetic fields, which governs the spin-related effect during OER. This explains the lower OER enhancement observed in N19 and N25. These results indicate that the enhanced OER is mainly from the remanence-state magnetization.

Discussion—Quantifying the OER increment: At first glance, the observed trend for the magnetization caused OER enhancement [Fig. 1(b)] differs from the one for domain wall occupancy (Appendix B). Such a discrepancy originates from the different magnetic anisotropy, which alters the domain structures at remanence. For $N < 10$, the domains are fully aligned in the saturated direction, as indicated by a high M_r after field removal. As the N increases, the decreased PMA weakens domain alignment, and domains of opposite magnetization are formed to minimize the magnetostatic energy. To examine the magnetic anisotropy effect, the OER is performed by magnetizing the sample along the hard axis (in-plane) under identical conditions (Supplemental Material Fig. 7 [22]). All films showed minimal OER enhancement under in-plane magnetization compared to out-of-plane. When the magnetic field is removed after hard-axis magnetization, the magnetization of the saturated film will go into random directions along the easy axis. Therefore, the spin-polarized OER can only be facilitated by orienting most of the magnetization along the easy axis.

To assess domain evolution in PMA films, the MOKE and MFM images were taken after applying and removing an out-of-plane magnetic field (Supplemental Material Fig. 8 [22]). The films with different N show different levels of domain wall disappearance. For films with $N > 19$, the domain wall disappearance is minimal compared to the ac-demagnetized state [Fig. 2(a)]. However, for $N \leq 15$, domain walls have disappeared significantly, indicating dominant out-of-plane magnetization. Figure 2(b) shows the domain wall occupancy ratios for all the samples after ac demagnetization (DW_{ac}) and remanence (DW_{Rem}) conditions [Fig. 2(b)]. The difference between DW_{ac} and DW_{Rem} is plotted in Fig. 2(c). It can be noticed that this difference shows a peak for N15, which also showed the highest improvement of OER in our Letter. The

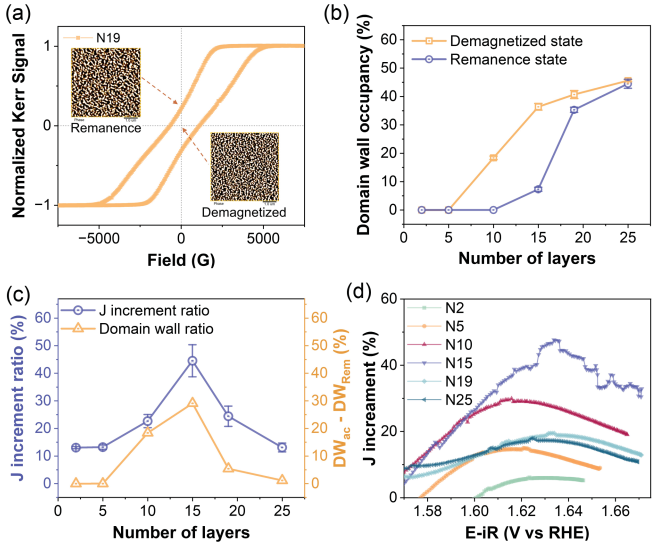


FIG. 2. (a) The MFM image at the demagnetized and remanence state, and the corresponding MOKE hysteresis loop for N19. (b) Calculated domain wall occupancy ratio at demagnetized and remanence state from MFM. (c) Quantitative correlation between OER increment ratio and the change in domain wall ratios from ac demagnetization (DW_{ac}) to remanence (DW_{Rem}) conditions. The error bars represent the standard deviation from three independent tests. (d) Potential-dependent OER enhancement ratio after magnetization.

trend of $DW_{ac} - DW_{Rem}$ shows a strong correlation to the trend of OER enhancement ratios, with a global ~12% offset, consistent with spin-unrelated effects described earlier. The correlation suggests that the OER enhancement by spin-related effects is mostly from the evolution of domain structures upon magnetization, aligning well with our previous observation in NiFe films [9], $CoFe_2O_4$ nanoparticles [29], and Fe_3O_4@$Ni(OH)_2$ catalysts [30].

To minimize the interference of expanded EDL by spin-unrelated effects, we further performed the OER with higher overpotential (1–1.7 V vs RHE) for the magnetized film. By applying a higher voltage, the enhancement at lower overpotential disappeared for all films, indicating less influence from the EDL. This can be attributed to the increased current density at higher overpotentials, which reduces the relative contribution of EDL expansion to the overall reaction performance. To compare the OER activities of "↑" and "↓" type domains, we successively perform the OER by positive and negative magnetization (Supplemental Material Fig. 9 [22]). The OER activities remain nearly unchanged with the magnetization direction. Minor differences may arise from the surface reconstruction or rise in temperature by the prolonged operation of the electromagnet (Supplemental Material Fig. 10 [22]). These results confirm the similar OER activity regardless of magnetization directions. This is expected, as magnetization only alters domain alignment without affecting individual spin orientations. The correlated OER activity with the domain structure indicates that the

aligned magnetic moment within the domain region affects the local spin-related interactions, which in turn influences reaction kinetics [31].

To further understand the spin-related OER enhancement, we analyze the enhancement effect across different overpotentials. The OER improvements after magnetization for all films begin near 1.57 V vs RHE, and reach a threshold at the range of 1.62–1.64 V vs RHE [Fig. 2(d)]. Such potential-dependent OER enhancement has also been found in previous works of Ni-foam [5] and Ni_1/MoS_2 [7] catalysts with threshold overpotentials of ∼1.58 and ∼1.53 V vs RHE, respectively, which has been attributed to the blockage of active sites or diffusion limitation by intense O_2 bubbling [5]. However, in our practice of premagnetization, the potential dependency could be caused by mixed factors, as we have minimized spin-unrelated enhancement. We note that the single-domain N2 and AFM CoOOH in the same condition did not show the threshold, instead, a plateau with a steady enhancement ratio is formed with increased overpotential, likely due to the enhanced mass transport and O_2 detachment by local magnetization-induced MHD effect. On the other hand, the threshold in OER enhancement only formed in the films with a change in domain walls, which involves spin-related effects. To probe the different enhancements with varied voltage, we compared the Tafel plots in different regions to study the OER kinetics. By magnetization, all films showed a decreased Tafel slope (Supplemental Material Fig. 11 [22]), indicating the facilitated reaction kinetics by aligning magnetic domains. The drop in Tafel slope taken from the threshold overpotentials follows the same trend with the activity enhancement ratios, whereas the Tafel slopes taken from higher voltage are less affected by magnetization (Supplemental Material Fig. 12 [22]).

It can be inferred from these results that the OER activities at different overpotentials may be dominated by different pathways, which show varied responses to the magnetization [6,10,32]. It has been reported that the spin-polarized O−O coupling is not the potential-limiting step (PLS) in the adsorbent evolution mechanism (AEM) pathway, whereas the spin-polarized catalysts can promote the intermolecular mechanism (I2M) involving the lattice oxygen [31]. Under AEM, although the electron transport can be affected by spin via spin-selective electron removal [11], dissociating *OOH toward oxygen turnover will pose a greater energy barrier, making the effect of spin negligible on the overall reaction rate. In contrast, under I2M, the formation of O_2 involves the coupling of oxygen species from two adjacent Co−O sites (Supplemental Material Fig. 13 [22]), which is strongly influenced by the spin alignment [11]. Within the magnetic domains, the aligned atomic magnetic moments from FM exchange interactions between Co sites favor spin alignment of Co−O radicals, which greatly reduces the energy barrier to produce triplet oxygen. The role of Co−O radical in the spin-related OER pathway is further validated by the pH-dependent study (Supplemental Material Fig. 14 [22]), where the enhancement effect by magnetization decreases at lower pHs. The M−O oxyl radicals are generated by the deprotonation of M−OH. This process will be facilitated as the *p*H of the electrolyte is higher than the pK_a of M−OH, explaining the *p*H dependency of magnetization-caused enhancement. Therefore, we attribute the formation of the threshold to the dominant I2M at moderate potential [33], while at higher potentials, the OER could shift toward the AEM pathway or become influenced by non-spin-related effects. These results highlight that the spin alignment, rather than specific spin orientation, plays a crucial role in facilitating spin-related OER enhancement. The spin orientation in the oxygen intermediates is defined by the direction of the intrinsic spin angular momentum of their electron (i.e., $+1/2$ and $-1/2$), which cannot be altered by the applied magnetic fields [34]. On the other hand, when spin alignment is established between neighboring Co−O radicals within magnetic domains, it promotes the O−O coupling for triplet oxygen production [31], which explains the influence of magnetization on OER enhancement.

Surface magnetism and atomic-level spin-related mechanism: Magnetic and structural characterizations for the multilayer film surface after OER are performed to understand the effect of surface magnetization on OER kinetics. As shown in Figs. 3(a)–3(f), all films (except single domain N2) show clear domain structure after OER, with minimal change in the domain size compared to the domain size before OER measurements. The magneto-optic Kerr effect (MOKE) magnetic hysteresis loops are also unchanged after OER except for N2, in which the PMA weakened (Supplemental Material Fig. 15 [22]). This indicates that the bilayer structure of Co/PtCo in N2 has been influenced by the surface reconstruction during OER [35,36], while the magnetic properties for other films remain similar after OER.

To probe the level of surface reconstruction in the multilayers, we show the cross-sectional HAADF-STEM image for N25 after OER [Fig. 3(g)]. The bulk layered structure can be well retained, and a thin reconstruction layer of ∼2 nm could be observed on the surface, which explains the weakened PMA in N2 (∼1.8 nm magnetic layers). The TEM profile also shows that at least 22 bilayers in N25 can be preserved after OER treatment (Supplemental Material Fig. 16 [22]). Besides, the uniform surface reconstruction is characterized by the minimal change in surface roughness from AFM results after OER (Supplemental Material Fig. 17 [22]).

The chemical compositions of the multilayer surface after OER are also characterized by the ARXPS, which indicates the formation of oxyhydroxide species $Co(Pt)O_xH_y$ on the surface (Supplemental Material Figs. 18 and 19 [22]). These results provide evidence of the presence of the spin pinning effect between the surface $Co(Pt)O_xH_y$ and bulk multilayers,

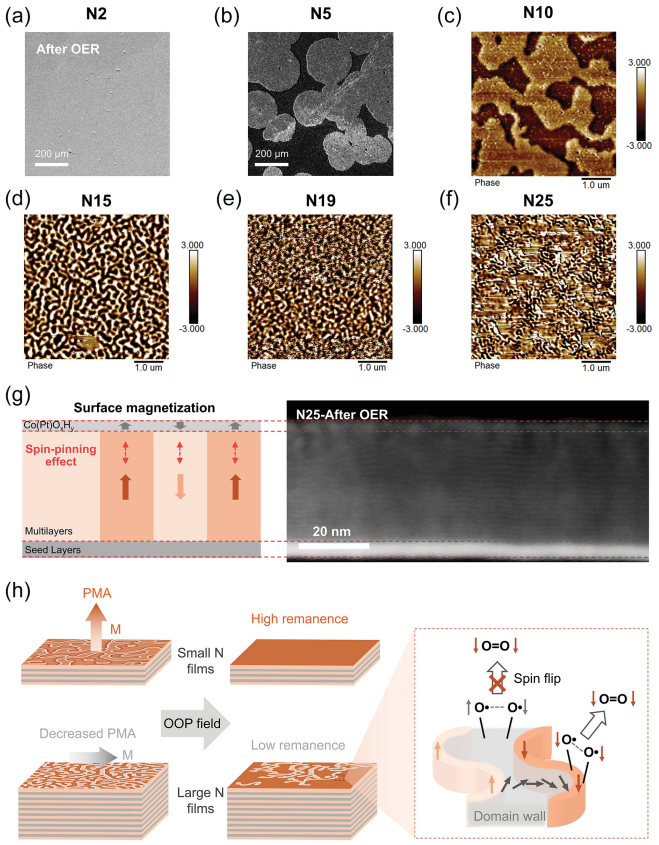


FIG. 3. (a),(b) The MOKE images of the ac-demagnetized N2 and N5 after OER. (c)–(f) The MFM images of the ac-demagnetized N10–N25 after OER. (g) The illustration of the spin pinning effect at the interface of the film-oxyhydroxide heterostructure, and the cross-sectional HAADF-STEM image for N25 after OER. (h) Illustration of the change of PMA in multilayer with different N, and the relative OER activity on domain and domain walls by atomic level O−O coupling. Magnetization (M).

which aligns the spins in Co(Pt)O_xH_y with the underneath Co/PtCo with interlayer exchange coupling [Fig. 3(g)] [10,37,38]. The reconstruction layer thickness of ∼3.9 nm (equivalent to three bilayers) is within the effective length of the spin pinning effect (∼5 nm) [37], which confirms that the surface Co(Pt)O_xH_y magnetization is affected by the multilayers and explains the clear domain structure in MFM. With spin pinning, the spins at the surface Co species become aligned in the domain regions, which in turn facilitates the alignment of *OH and *O species on the Co sites through short-range spin exchange interaction [7]. As a result, the O−O coupling at the ferromagnetic coupled domain region can happen with a lower energy barrier for the triplet-state oxygen ($\uparrow O = O \uparrow$) turnover [Fig. 3(h)]. This further explains the similar OER enhancement ratio observed with positive and negative magnetization. The similar OER activity in "↑" and "↓" type domains indicates that the spin-related OER is primarily associated with the spin alignment between active sites under the I2M pathway. The domain wall region, on the other hand, is regarded as the transition of the "↑" and "↓" type long-range magnetization, in which the spins of Co sites tend to be disordered. In this case, the O−O coupling happens between the spin-disordered O species, resulting in a higher energy barrier to produce triplet oxygen [31]. Accordingly, the lower OER activity in domain wall regions exactly matches the quantitative correlation between the spin-related OER enhancement and the change in domain wall ratios.

Based on this understanding, we highlight the crucial role of PMA in governing the domain structures at remanence state and optimizing spin-related interactions for enhancing OER [Fig. 3(h)]. In the films with higher PMA, the well-aligned OOP magnetic moments lead to an extended FM coupled domain region, where the spin-aligned Co sites promote the O−O coupling via I2M pathway. Meanwhile, the moderate E_M for lower N films also leads to a high M_r, which enables a high degree of domain alignment at remanence state to enhance OER. Therefore, the OER enhancement for multilayer films upon magnetization is determined by both PMA and domain wall density. In our Co/PtCo multilayers, the OER enhancement peaks at N15, suggesting a balance between high domain wall density to enable a pronounced OER enhancement and maintaining the domain alignment for efficient spin-related OER kinetics. For $N < 15$, the high PMA enables high domain alignment, but the low E_M results in low domain wall occupancy. On the other hand, when $N > 15$, the high E_M in the multilayer system weakens PMA and leads to the inability to maintain the domain alignment at the remanence state, although the domain wall density greatly increases.

Conclusions—In conclusion, this Letter demonstrates the critical role of perpendicular magnetic anisotropy in enabling stable, magnetic-field-free spin-enhanced OER. By systematically tuning PMA through varying bilayer numbers, we establish a direct numerical correlation between the spin-enhanced OER by premagnetization and the change in domain wall ratio at remanence state, while effectively excluding the global spin-unrelated effects. The optimal OER enhancement ratio at N15 highlights the necessity of balancing PMA, which stabilizes the aligned domains, with sufficient domain wall density to enhance OER upon magnetization. For $N < 10$, the PMA increases with N by the dominant interface, which favors the OER enhancement by the enhanced domain wall occupancy. However, as the N increases above 10, the domain occupancy gradually increases while PMA starts to decrease due to the enhanced magnetostatic energy, which reduces remanent magnetization and the OER enhancement. Overall, by introducing PMA into magnetic OER catalysts, this Letter not only resolves previous challenges in identifying spin-related enhancement in OER by magnetization but also provides a new direction for applying magnetic stability to achieve magnetic-field-free spin-enhanced OER.

Acknowledgments—This work was financially supported by the Ministry of Education, Singapore, through a Tier 2 grant (MOE-T2EP10223-0006). S. N. P. would like to acknowledge the financial support by the Ministry of Education, Singapore, under its Tier 2 grant MOET2EP50122-0023 and the National Research Foundation (NRF), Singapore, for the CRP21 grant (NRFCRP21-2018-0003). The authors appreciate the "Facility for Analysis, Characterisation, Testing and Simulation" in Nanyang Technological University for materials characterizations.

Z. J. X. and A. Y. conceived the original idea. S. N. P., Z. J. X., A. Y., and D. K. designed the research. D. K. and H. R. prepared the thin films. A. Y. performed most of the characterizations. Z. G., A. Y., and D. K. conducted the micromagnetic simulations. D. K., A. Y., and H. R. contributed to the MOKE. L. T. performed the XPS. P. S. and A. Y. conducted the TEM. R. M. and P. K. M. assisted with the VSM. A. Y., D. K., S. N. P., and Z. J. X. wrote the paper. T. W. contributed to the revision. X. R. W. provided theoretical support.

The authors declare no competing interests.

Data availability—The data that support the findings of this article are openly available [39].

[1] M. T. M. Koper, J. Electroanal. Chem. **660**, 254 (2011).
[2] M. T. M. Koper, Chem. Sci. **4**, 2710 (2013).
[3] J. Gracia, Phys. Chem. Chem. Phys. **19**, 20451 (2017).
[4] J. Gracia, J. Phys. Chem. C **123**, 9967 (2019).
[5] F. A. Garcés-Pineda, M. Blasco-Ahicart, D. Nieto-Castro, N. López, and J. R. Galán-Mascarós, Nat. Energy **4**, 519 (2019).
[6] X. Ren *et al.*, Nat. Commun. **12**, 2608 (2021).
[7] T. Sun *et al.*, Nat. Nanotechnol. **18**, 763 (2023).
[8] E. van der Minne *et al.*, Appl. Phys. Rev. **11**, 011420 (2024).
[9] X. Ren, T. Wu, Z. Gong, L. Pan, J. Meng, H. Yang, F. B. Dagbjartsdottir, A. Fisher, H.-J. Gao, and Z. J. Xu, Nat. Commun. **14**, 2482 (2023).
[10] T. Wu *et al.*, Proc. Natl. Acad. Sci. U.S.A. **121**, e2318652121 (2024).
[11] T. Wu and Z. J. Xu, Curr. Opin. Electrochem. **30**, 100804 (2021).
[12] S. Bhatti, R. Sbiaa, A. Hirohata, H. Ohno, S. Fukami, and S. N. Piramanayagam, Mater. Today **20**, 530 (2017).
[13] S. Ma, Q. Fu, J. Han, T. Yao, X. Wang, Z. Zhang, P. Xu, and B. Song, Adv. Funct. Mater. **34**, 2316544 (2024).
[14] S. Luo, K. Elouarzaki, and Z. J. Xu, Angew. Chem., Int. Ed. **61**, e202203564 (2022).
[15] D. Kumar *et al.*, Phys. Rep. **958**, 1 (2022).
[16] S. N. Piramanayagam, J. Appl. Phys. **102**, 011301 (2007).
[17] R. Sbiaa, H. Meng, and S. N. Piramanayagam, Phys. Status Solidi RRL **5**, 413 (2011).
[18] F. J. den Broeder, D. Kuiper, A. P. van de Mosselaer, and W. Hoving, Phys. Rev. Lett. **60**, 2769 (1988).
[19] Q. Huang, S. Xie, J. Hao, Z. Ding, C. Zhang, H. Sheng, and J. Zhao, Angew. Chem., Int. Ed. **62**, e202300469 (2023).
[20] S. T. Lim, M. Tran, J. W. Chenchen, J. F. Ying, and G. Han, J. Appl. Phys. **117**, 17A731 (2015).
[21] M. Arora, R. Hübner, D. Suess, B. Heinrich, and E. Girt, Phys. Rev. B **96**, 024401 (2017).
[22] See Supplemental Material at http://link.aps.org/supplemental/10.1103/bdr5-bg1j for a complete discussion of methods, characterization results, simulation results, and electrochemical analysis, which includes Refs. [23–28].
[23] Z. Chen, C. X. Kronawitter, Y.-W. Yeh, X. Yang, P. Zhao, N. Yao, and B. E. Koel, J. Mater. Chem. A **5**, 842 (2017).
[24] W. Eberhardt, P. Fayet, D. M. Cox, Z. Fu, A. Kaldor, R. Sherwood, and D. Sondericker, Phys. Rev. Lett. **64**, 780 (1990).
[25] J. J. Joos, P. Bassirian, P. Gypens, J. Mulkers, K. Litzius, B. Van Waeyenberge, and J. Leliaert, J. Appl. Phys. **134**, 171101 (2023).
[26] Y. Tong, P. Chen, T. Zhou, K. Xu, W. Chu, C. Wu, and Y. Xie, Angew. Chem., Int. Ed. **56**, 7121 (2017).
[27] A. Vansteenkiste, J. Leliaert, M. Dvornik, M. Helsen, F. Garcia-Sanchez, and B. Van Waeyenberge, AIP Adv. **4**, 107133 (2014).
[28] C. Wei, S. Sun, D. Mandler, X. Wang, S. Z. Qiao, and Z. J. Xu, Chem. Soc. Rev. **48**, 2518 (2019).
[29] J. Ge, X. Ren, R. R. Chen, Y. Sun, T. Wu, S. J. H. Ong, and Z. J. Xu, Angew. Chem., Int. Ed. **62**, e202301721 (2023).
[30] J. Ge, R. R. Chen, X. Ren, J. Liu, S. J. H. Ong, and Z. J. Xu, Adv. Mater. **33**, e2101091 (2021).
[31] T. Wu *et al.*, Proc. Natl. Acad. Sci. U.S.A. **121**, e2318652121 (2024).
[32] Y.-H. Fang and Z.-P. Liu, ACS Catal. **4**, 4364 (2014).
[33] M. J. Craig, G. Coulter, E. Dolan, J. Soriano-Lopez, E. Mates-Torres, W. Schmitt, and M. Garcia-Melchor, Nat. Commun. **10**, 4993 (2019).
[34] Y. B. Zel'dovich, A. L. Buchachenko, and E. L. Frankevich, Phys. Usp. **31**, 385 (1988).
[35] C. Luan *et al.*, Angew. Chem., Int. Ed. **62**, e202305982 (2023).
[36] C. Luan, M. Corva, U. Hagemann, H. Wang, M. Heidelmann, K. Tschulik, and T. Li, ACS Catal. **13**, 1400 (2023).
[37] T. Wu *et al.*, Nat. Commun. **12**, 3634 (2021).
[38] M. Lu, Y. Du, S. Yan, T. Yu, and Z. Zou, Phys. Rev. Lett. **133**, 258001 (2024).
[39] A. Yu, D. Kumar, Z. Gong, L. Tannesia, H. Rahaman, P. Song, T. Wu, R. Maddu, P. K. Mishra, X. R. Wang, S. N. Piramanayagam, and Z. J. Xu, Zenodo, 2026, 10.5281/zenodo.18180979.
[40] T. Reier, M. Oezaslan, and P. Strasser, ACS Catal. **2**, 1765 (2012).
[41] S. McVitie *et al.*, Sci. Rep. **8**, 5703 (2018).
[42] P. Chowdhury, P. D. Kulkarni, M. Krishnan, H. C. Barshilia, A. Sagdeo, S. K. Rai, G. S. Lodha, and D. V. Sridhara Rao, J. Appl. Phys. **112**, 023912 (2012).
[43] S. Kaneko, R. Myochi, S. Takahashi, N. Todoroki, T. Wadayama, and T. Tanabe, J. Phys. Chem. Lett. **8**, 5360 (2017).
[44] A. S. Aricò, A. K. Shukla, H. Kim, S. Park, M. Min, and V. Antonucci, Appl. Surf. Sci. **172**, 33 (2001).
[45] Y. Duan *et al.*, Angew. Chem., Int. Ed. **60**, 7418 (2021).

[46] M. C. Biesinger, B. P. Payne, A. P. Grosvenor, L. W. M. Lau, A. R. Gerson, and R. S. C. Smart, Appl. Surf. Sci. **257**, 2717 (2011).
[47] C. W. Scheeren, G. Machado, S. R. Teixeira, J. Morais, J. B. Domingos, and J. Dupont, J. Phys. Chem. B **110**, 13011 (2006).
[48] P. F. Carcia, J. Appl. Phys. **63**, 5066 (1988).
[49] C. J. Lin, G. L. Gorman, C. H. Lee, R. F. C. Farrow, E. E. Marinero, H. V. Do, H. Notarys, and C. J. Chien, J. Magn. Magn. Mater. **93**, 194 (1991).
[50] J. W. Knepper and F. Y. Yang, Phys. Rev. B **71**, 224403 (2005).
[51] R. Sbiaa, Z. Bilin, M. Ranjbar, H. K. Tan, S. J. Wong, S. N. Piramanayagam, and T. C. Chong, J. Appl. Phys. **107**, 103901 (2010).
[52] V. Grolier *et al.*, Phys. Rev. Lett. **71**, 3023 (1993).
[53] J. Chatterjee, T. Tahmasebi, S. Mertens, G. S. Kar, T. Min, and J. D. Boeck, IEEE Trans. Magn. **50**, 1 (2014), https://ieeexplore.ieee.org/document/6971467.
[54] P. J. H. Bloemen and W. J. M. de Jonge, J. Magn. Magn. Mater. **116**, L1 (1992).
[55] F. J. A. den Broeder, W. Hoving, and P. J. H. Bloemen, J. Magn. Magn. Mater. **93**, 562 (1991).
[56] M. T. Johnson, R. Jungblut, P. J. Kelly, and F. J. A. den Broeder, J. Magn. Magn. Mater. **148**, 118 (1995).
[57] K. Janicka, J. D. Burton, and E. Y. Tsymbal, J. Appl. Phys. **101**, 113921 (2007).
[58] C. Kittel, Phys. Rev. **70**, 965 (1946).
[59] M. T. Johnson, P. J. H. Bloemen, F. J. A. d. Broeder, and J. J. d. Vries, Rep. Prog. Phys. **59**, 1409 (1996).

End Matter

Appendix A: $(\mathrm{Co/PtCo})_{N-1}$ *multilayers preparation and characterization*—The schematic of the stack utilized in the study is presented in Supplemental Material [22]. The deliberate alloying Co in the PtCo layer is to introduce more Co active sites for OER, owing to the low activity of bulk Pt [40]. The lamination of $\mathrm{Ta(3)/Pt(5)/[Co(0.5)/PtCo(0.8)]}_{N-1}\mathrm{Co(0.5)}$ (thicknesses in nm) multilayers are grown on a thermally oxidized Si substrate by dc magnetron sputtering. Here, the Ta(3) is used as a seed layer to improve the adhesion quality of the multilayers and Pt(5) is used to enhance the (111) texture and the anisotropy of Co/PtCo multilayers further [20]. Details on the preparation of multilayers can be found in the Supplemental Material [22].

We first characterize the structural properties of the as-prepared films (Supplemental Material Figs. 20–23 [22]). Bright-field transmission electron microscopy (BFTEM) and high-angle annular dark-field scanning transmission electron microscopy (HAADF-STEM) imaging were adopted to identify the layered structures [41]. The cross-sectional BFTEM and HAADF-STEM image for sample with $N = 25$ (denoted as N25) shows the well-grown layered structure with bright (Co) and darker (PtCo) layers through the film. The 24 repeats of [Co/PtCo] stackings in N25 can also be observed in the corresponding BFTEM thickness profile, in which the period of ∼1.2 nm matches with the bilayer [Co/PtCo] thickness. The energy-dispersive x-ray spectroscopy (EDS) showed the homogeneous dispersion of Co and the layered distribution of Pt in the multilayer. The crystal structures in $(\mathrm{Co/PtCo})_{N-1}$ multilayers are characterized by x-ray diffraction (XRD). As shown in Supplemental Material Fig. 19(g) [22], the peaks match with the Co, Pt, CoPt, and CoO phases in the sample. Notably, reducing the number of bilayers shifts PtCo(111) to lower 2θ, attributing to the strain (ε) from lattice mismatch between the seed layer Pt and Co layer [21,42,43]. The interfacial strain leads to the expansion of CoPt lattice up to 5.28% in N2 sample (Supplemental Material Fig. 22 [22]), which enhances PMA. The surface quality of the as-deposited films is characterized by atomic force microscopy (AFM) under ScanAsyst mode, which shows a small surface roughness (0.213–0.410 nm) (Supplemental Material Fig. 23 and Table 1 [22]). Additionally, the angle-resolved x-ray photoelectron spectroscopic (ARXPS) of all films indicates the naturally oxidized surface of Co capping layer ($\mathrm{CoO_x}$), the metallic Co feature near ∼778.19 eV gradually disappeared from bulk to surface [Supplemental Material Figs. 20(h) and 24–29 [22]]. At 0° tilting angle, Co $2p$ and Pt $4f$ spectra of the multilayers reveal the unchanged chemical composition in the bulk films as N increases. Co $2p$ XPS spectra exhibit the characteristic multiplet-split envelope of dominant $\mathrm{Co^{2+}}$ species and metallic Co species [44–46]. The Pt in PtCo layer stays mostly at metallic state, evidenced by the dominant $\mathrm{Pt^0}$ peaks at 74.59 and 71.49 eV for Pt $4f_{5/2}$ and Pt $4f_{7/2}$, respectively [47]. As the tilting angle increases, peak positions for Co $2p$ and Pt $4f$ spectra remain unchanged, which indicates the identical chemical composition from bulk to surface in $(\mathrm{Co/PtCo})_{N-1}$. The Co alloying ratio in bulk PtCo layers is estimated from the ARXPS results of $N > 10$ samples [Supplemental Material Fig. 19(i) [22]] due to the interference of the Pt seed layer for $N < 10$, where the Co/Pt ratio in the PtCo layers is estimated to be 1.5∶1.

Appendix B: Perpendicular magnetic anisotropy and magnetic domains—A Pt/Co multilayer system can exhibit strong perpendicular magnetic anisotropy when the Co layer thickness decreases to only a few atomic layers [48,49]. The PMA in such heterostructures originates from the orbital hybridization of orbitals corresponding to Co and Pt at the Co/Pt interface and the strength of PMA can be tailored by altering the number of bilayers [50,51]. The PMA can be further enhanced by

using suitable seed layers such as Ta/Pt below the multilayers. The magnetic properties were first examined by measuring magnetic hysteresis (M-H) loops using Kerr microscopy (in polar mode) and vibrating sample magnetometer (VSM). Typical rectangular M-H loops were obtained for multilayers with N up to 10 [Fig. 4(a)], indicating sharp magnetization switching through relatively faster domain wall motion [50]. As N increases above 10, a tail near coercivity (H_C) in the M-H loops appears and becomes more significant in N19 and N25, resulting in decreased M_r [Fig. 4(a), inset]. Such a trend is in agreement with the previously reported magnetic multilayers, where the slanted loops in higher N samples were attributed to the enhanced barrier energy (E_B) and magnetostatic energy by strong interlayer coupling [51]. Moreover, the magnetization reversal process in N15–N25 may happen in two steps: nucleation of the large-number domains followed by their slow expansion [51,52]. To quantify the strength of the PMA, the anisotropy constant (K_u) is calculated from $K_{\text{eff}} = K_u - (1/2)^* \mu_0 M_S^2$, where the effective uniaxial anisotropy constant (K_{eff}) is estimated from the integral over the difference from the out-of-plane and in-plane M-H loops (Supplemental Material Fig. 30 [22]) [53,54]. The positive K_u for N below 25 indicates the PMA in the films, whereas the small negative K_u for N25 suggests a decreased PMA. As shown in Fig. 4(b), the value of K_u peaks at N10 and gradually decreases as the bilayer number increases. The K_u is normally affected by the volume (K_V) and interfacial anisotropy (K_S), based on $K_u = K_V + 2K_S/t$ [55], where K_V contains contributions from magnetocrystalline (K_{MC}) and magnetoelastic anisotropy (K_{ME}). For N below 10, where strong lattice strain contributes to K_{ME}, the stacking of multilayers introduces more interfaces, enhancing the PMA [21]. As N further increases, the strain relaxation reduces K_{ME}, leading to the decrease of K_u. Besides, the interdiffusion of Co and Pt in higher N films may also weaken the K_S, leading to a transition from interface-dominated anisotropy to a more bulklike behavior, which also decreases PMA by large magnetostatic energy [55,56]. Despite this reduction, all films with $N > 10$ showed sharp maze domains [Figs. 4(f)–4(i)], indicating the presence of PMA.

We further analyze the domain structure of the studied samples at ac-demagnetized state. The size of the magnetic domains, measured using Kerr microscopy (in polar mode) and magnetic force microscopy (MFM), gradually decreases from micrometer to nanometer-scale as N increases [Figs. 4(c)–4(i)]. We use the Kerr microscopy to obtain the domain structures of N2 and N5 films as the domains are much larger (~100 μm range) and these sizes are unsuitable for MFM measurements with a limited scan size. For N2, no contrast in the domain structure can be seen at the demagnetized state, which could be regarded as having a domain larger than the range of Kerr measurements

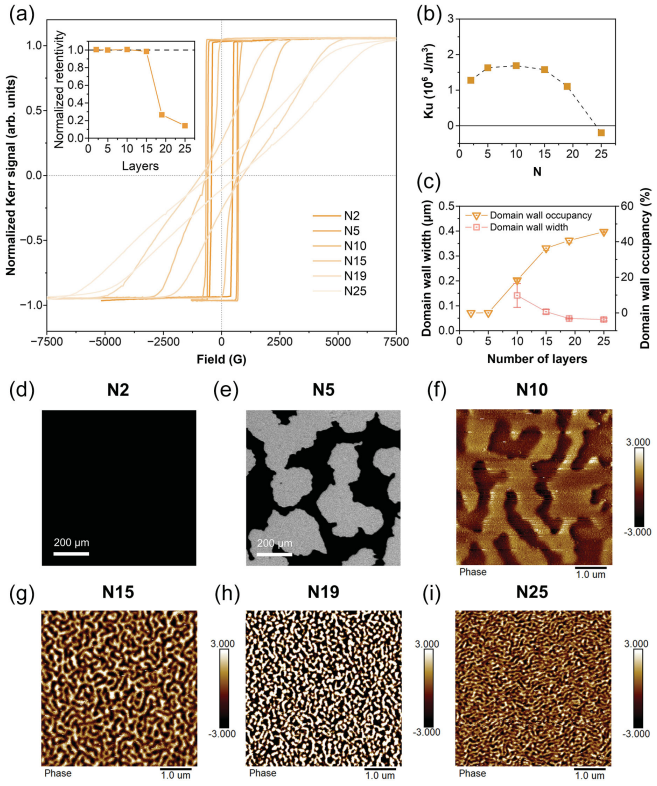


FIG. 4. (a) MOKE hysteresis loops for as-prepared films. The inset is the normalized retentivity of films normalized by Kerr intensity corresponding to the saturated state. (b) The magnetic anisotropy (K_u) as a function of number of bilayers. (c) The change in domain wall width and the wall occupancy area ratio with the number of bilayers. (d),(e) The MOKE and (f)–(i) MFM images of ac-demagnetized films.

(~1 mm). For N5, the domain structure can be clearly seen in the demagnetized image, with a large domain size of ~200 μm scale. Similar domain patterns with decreased domain size are observed in the MFM patterns and micromagnetic simulation results when N further increases (Supplemental Material Figs. 31 and 32 [22]), which are related to the magnetostatic interactions induced by magnetic layer stacking [57,58]. Besides, the estimated domain wall width (δ) also showed a decreasing trend as N increases [Fig. 4(c)], which could be explained by the balance between magnetostatic energy (E_M) and domain wall energy (E_{dw}) [51,57]. The total magnetostatic energy (E_M) in the ultrathin multilayers consists of intralayer (E_M^{intra}) and interlayer (E_M^{intra}) components [51,57], but in our case of Co/PtCo multilayer it can simply to E_M^{intra} due to the minimal separation ($d \approx 0$) between magnetic layers. Previous works suggest the decreased domain wall width (L) lead to a decrease E_M^{intra} in the system with a higher number of bilayers, but increases the E_{dw} [51,57]. The equilibrium domain size is thus determined by the minimized total energy in the system $E = E_M^{\text{intra}} + E_{dw}$, which normally shows an exponential

decrease with N [51,57]. Moreover, such nanometer-scale domains in higher N will increase magnetostatic interaction between domains [59].

Because of the critical role of domain wall occupancy in magnetization-caused OER enhancement [9,29,30], the area of domain walls of the multilayers at ac-demagnetized states are directly calculated from the MFM images. The domain wall region is defined as the transition between the "up (↑)" and "down (↓)" domains (Supplemental Material Fig. 33 [22]). The domain wall occupancy ratios, estimated from the portion of domain wall area to the whole surface, gradually increase up to ∼45% [Fig. 4(c)].